Supplementary Information

Exchange coupling in a frustrated trimetric molecular magnet reversed by a 1D nano-confinement

Oleg Domanov,[1] Eugen Weschke,[2] Takeshi Saito,[3] Herwig Peterlik,[1] Thomas Pichler,[1] Michael Eisterer,[4] Hidetsugu Shiozawa[1,5*]

[1]Faculty of Physics, University of Vienna, Boltzmanngasse 5, 1090 Vienna, Austria

[2]Helmholtz-Zentrum Berlin für Materialien und Energie GmbH, Albert-Einstein-Str. 15, 12489 Berlin, Germany

[3]Nanomaterials Research Institute, National Institute of Advanced Industrial Science and Technology (AIST), 1-1-1 Higashi, Tsukuba 305-8565, Japan

[4]Atominstitut, TU Wien, Stadionallee 2, 1020 Vienna, Austria

[5]J. Heyrovsky Institute of Physical Chemistry, Czech Academy of Sciences, Dolejskova 3, 182 23 Prague 8, Czech Republic

[*]To whom correspondence should be addressed; E-mail: hidetsugu.shiozawa@univie.ac.at & hide.shiozawa@jh-inst.cas.cz

1 Methods

1.1 Preparation of SWCNT films

SWCNT materials with mean diameters of 1.3, 1.7 and 2.1nm were synthesized by the enhanced direct injection pyrolytic synthesis (e-DIPS) [1]. Their toluene solution prepared by ultrasonication was filtered through a 2.5 cm diameter cellulose filter membrane with a pore diameter of 0.2 mm (Millipore) using a vacuum filtration setup. As soon as the toluene was evaporated, the SWCNT film was pealed off the membrane. The SWCNT films were subjected to a purification process at 1300° for 18 hours in high vacuum condition to remove magnetic impurities. Prior to the filling, defects were introduced to the SWCNTs by

oxidation in air at 500°C for 30 minutes.

1.2 Filling of SWCNT films with Ni(II) acetylacetonate

Ni(II) acetylacetonate powder (Sigma-Aldrich) were purified by vacuum sublimation at temperatures around 130°C and sealed together with the SWCNT film in a borosilicated glass ampule at a base preassure better than $1\times\ 10^{-5}$mbar. The SWCNTs film was heated together with the Ni(II) acetylacetonate within the ampule at 130°C for 160-280 hours [2, 3]. Then, the SWCNT film was taken out the ampule and heated at 130°C in a clean ampule in high vacuum for several hours to ensure the purity.

For Raman spectroscopy, the conversion of the 1D-Ni(acac)$_2$ into nickel nanoclusters and inner tubes was conducted in high vacuum conditions at 500°C for 2 hours.

1.3 X-ray diffraction

X-ray diffraction (XRD) measurements were carried out using a Bruker Nanostar equiped with a Vantec 2000 gas detector and a Fuji FLA 7000 image plate system at a x-ray wavelength of $\lambda = 0.154nm$ (CuK_α). 2D scattering data were azimuthally integrated to result in scattering intensities versus scattering angle 2θ. The Ni(II) acetylacetonate powder was held between two thin polymer (PE) films. The scattered intensity of the supporting film was minimal, nevertheless this background contribution was subtracted. The XRD scattering profile of the 3D-Ni(acac)$_2$ was constructed using the FullProf software package with lattice parameters found in literature[4]. SWCNT films were folded and measured in a freestanding configuration.

1.4 X-ray photoemission spectroscopy

X-ray photoemission spectroscopy (XPS) measurements were carried out using a custom setup ($1\times\ 10^{-10}$mbar) equipped with a monochromatic Al K_α radiation (1486.6 eV) source and a hemispherical SCIENTA RS4000 photoelectron analyzer. The experimental energy resolution was better than 500meV. The Ni/C atomic ratio was calculated from the area intensity ratios of the Ni2p and the C1s peaks considering the photoionisation cross section.

The line shape analysis was done by using a Donijac-Sunij (DS) function[5] folded with a Gauss-Laurenzian (GL) for the main peak and GL functions for the higher binding energy components after Shirley[6] background subtraction.

1.5 Raman spectroscopy

Raman measurements were carried out in ambient conditions with a Bruker FT Raman spectrometer at a laser wavelength (energy) of 1064 nm (1.165eV).

1.6 Magnetisation measurements

The bulk magnetisation data were recorded at temperatures between 2K and 300K at applied magnetic fields up to 1T. The SWCNT film was mounted in a plastic straw, which added no noticable background signal to the data. XMCD measurements were carried out at UE46-PGM-1 variable polariasation undulator beamline at BESSY II, Helmoholz-Zentrum Berlin. XMCD spectra were recorded by measuring the sample drain current across the Ni 2p edges with the photon helicity parallel (μ^+) or antiparallel (μ^-) to the magnetic field applied to the sample at a sample temperature of 4.16K in magnetic fields up to 6T.

2 Confirmation of $Ni(acac)_2$ inside SWCNTs by Raman spectroscopy

The encapsulation of the $Ni(acac)_2$ within the SWCNTs is verified by Raman spectroscopy. Figure S1 shows the SWCNT's radial breathing mode (RBM) of the 1D-$Ni(acac)_2$@NT1.3 before and after annealing in vacuum at 500°C for 2 hours. Here, the RBM frequency is inversely proportional to the SWCNT diameter; the response of smaller (larger) diameter tubes is at higher (lower) wavenumber. Before the annealing, the RBM spectrum is dominated by the main peak around a Raman shift of 175cm^{-1} steming from the outer tubes. After the annealing, the peaks in the region above 280cm^{-1} dominates the spectrum. These intensified RBM lines are of the inner tubes grown from the 1D-$Ni(acac)_2$ inside SWCNTs[2, 3].

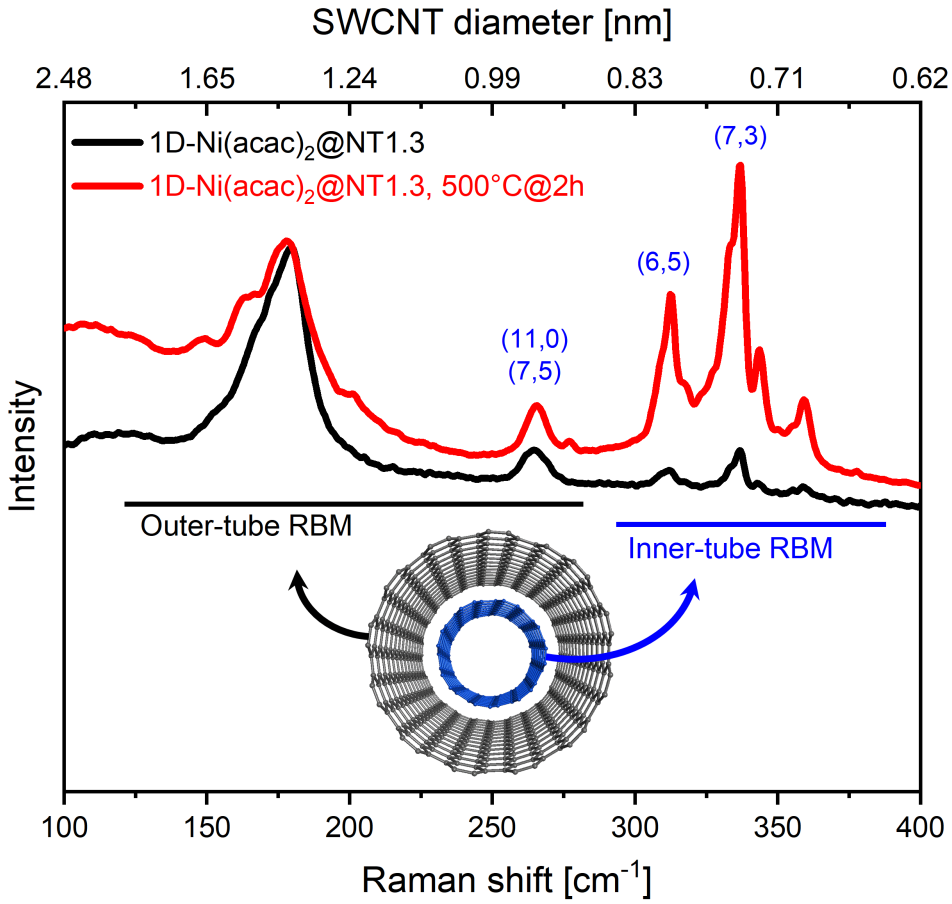

Figure S 1: The Raman spectra of the 1D-Ni(acac)$_2$@NT1.3 before and after annealing in vacuum at 500°C for 2 hours in the radial breathing mode (RBM) region. The RBM signals for narrow tubes located at frequencies above 290cm^{-1} are enhanced upon annealing due to the formation of inner tubes.

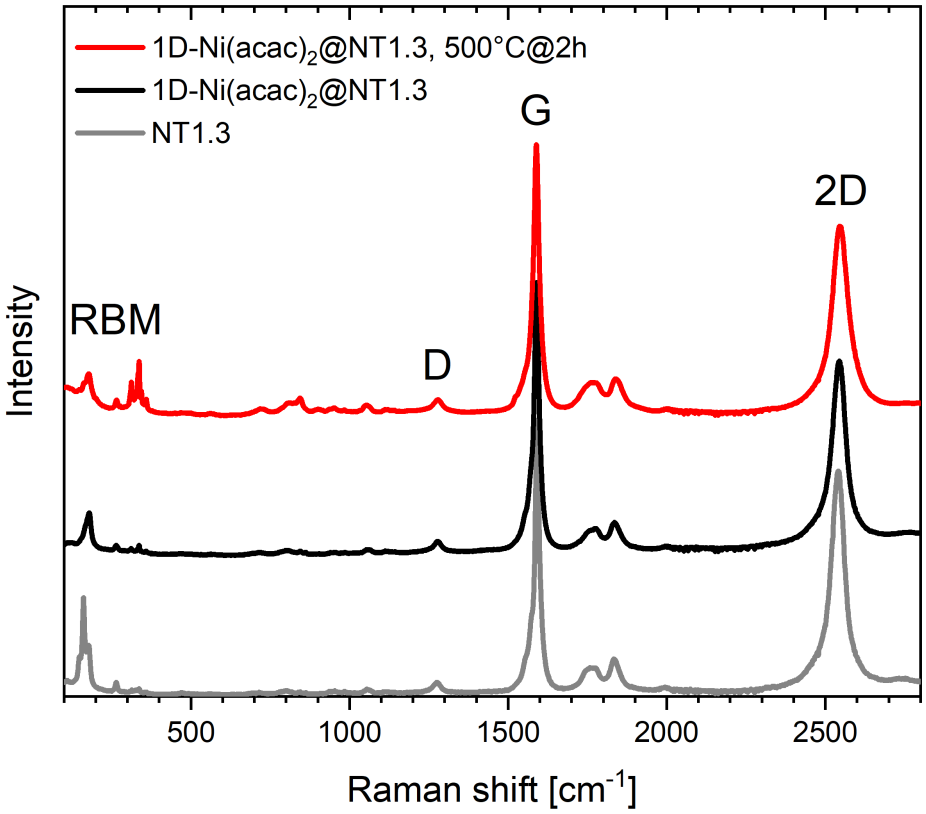

Figure S 2: Raman spectra in the D and G mode region for the 1D-Ni(acac)$_2$@NT1.3 before and after vacuum heating at 500°C for 2 hours.

The samples display a small ratio of the D to G line and thus a low amount of defects for a given tube length.

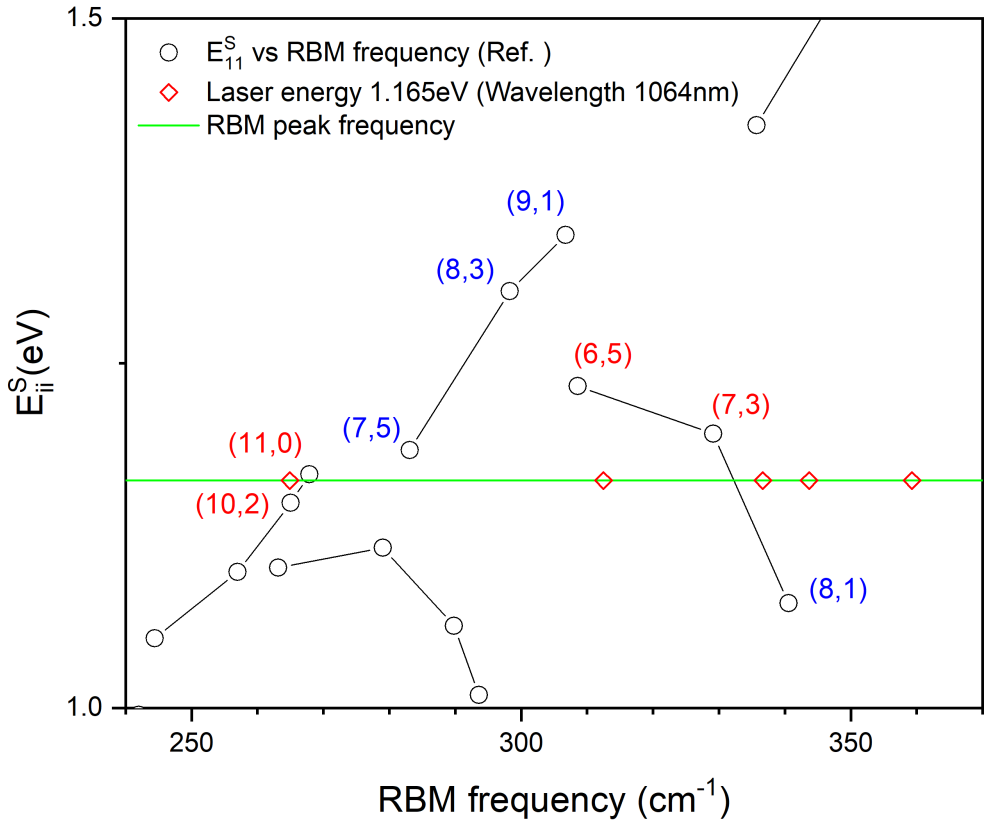

Figure S3: Kataura plot relating the optical transition energy between Van Hove singularity peaks and the RBM frequency of single-wall carbon nanotubes [7]. The dashed horizontal line is 1064 nm (1.165eV) laser energy used for the present Raman study. The RBM peak frequencies assigned for the 1D-Ni(acac)$_2$@NT1.3 after annealing in vacuum at 500°C for 2 hours are plotted as open diamonds.

3 SQUID data analysis

3.1 SWCNT background subtraction

The magnetisation data of the NT1.3 and NT2.1 containing minimal ferromagnetic impurities were measured, scaled and subtracted from the magnetisation data of the 1D-Ni(acac)$_2$@NT1.3 and 1D-Ni(acac)$_2$@NT2.1, respectively, such that the hysteretic background could be eliminated. An example for the Ni-AcAc@NT1.3 is shown in Fig. S4.

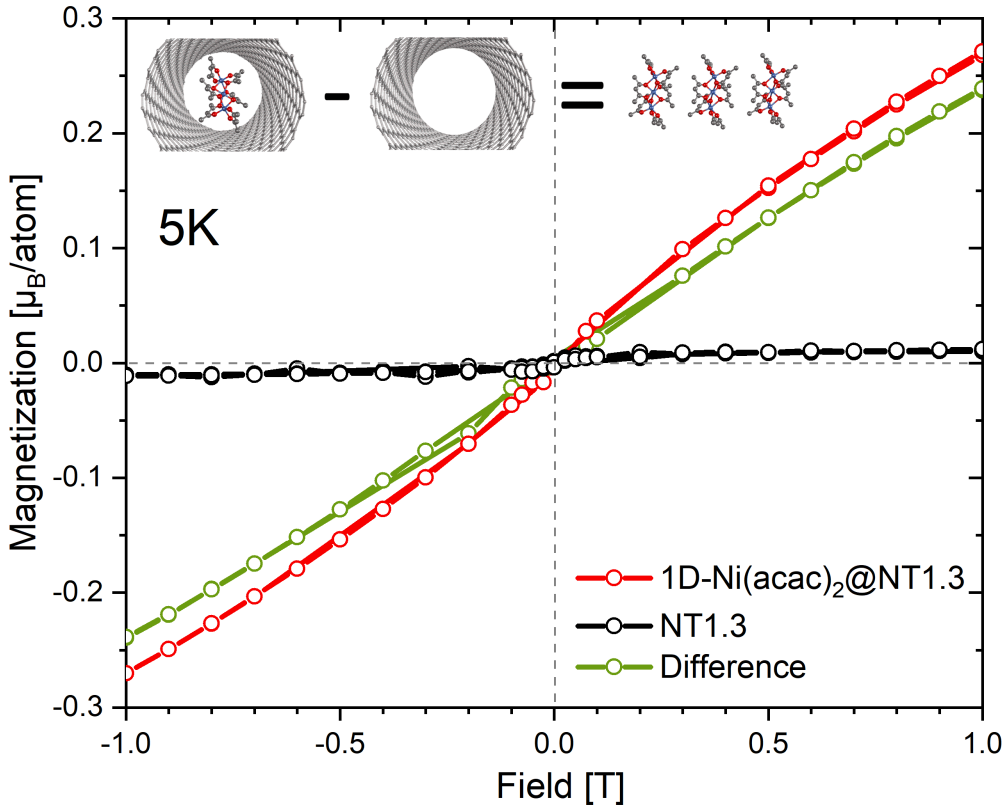

Figure S 4: SWCNT's background subtraction from the magnetisation data of the 1D-Ni(acac)$_2$@NT1.3.

The influence of exposure to atmosphere of the SWCNTs where the interior nanospace was made accessible by heating in air is shown in Fig. S5 and compared to the same sample after vacuum heat treatment and subsequent handling and measurement under argon atmosphere.

The exposure to air results in a greatly increased magnetisation with a shape that is typical for a phase transition. Considering the temperature range, we can conclude, that the origin of this signal is indeed the liquid-solid phase transition of oxygen.

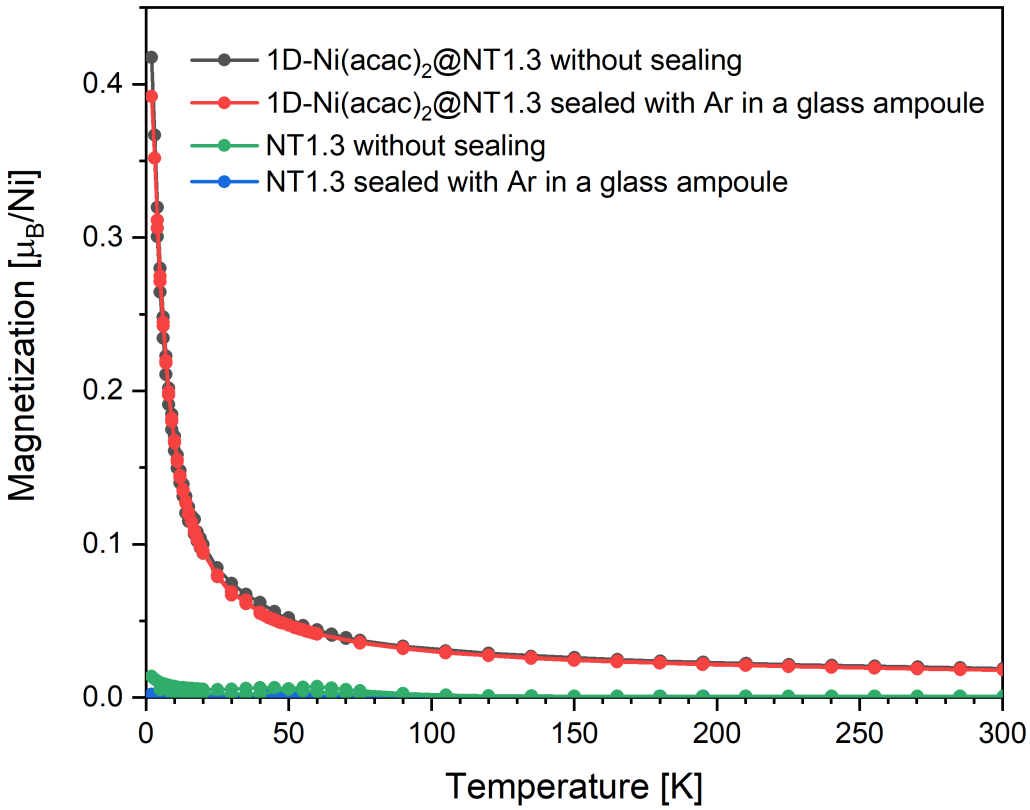

Figure S 5: Temperature-dependent magnetisation data of the 1D-Ni(acac)$_2$@NT1.3 and pristine NT1.3, with and without sealing with Ar.

3.2 Magnetisation curves at different temperatures

Figure S6 shows the field-dependent magnetisation data of the 3D-Ni(acac)$_2$ measured at 2, 5, 50 and 300K. The saturation is significant at 2K, hence the analysis on the effetive magnetic moment and susceptibility has been carried out at temperatures above 5K.

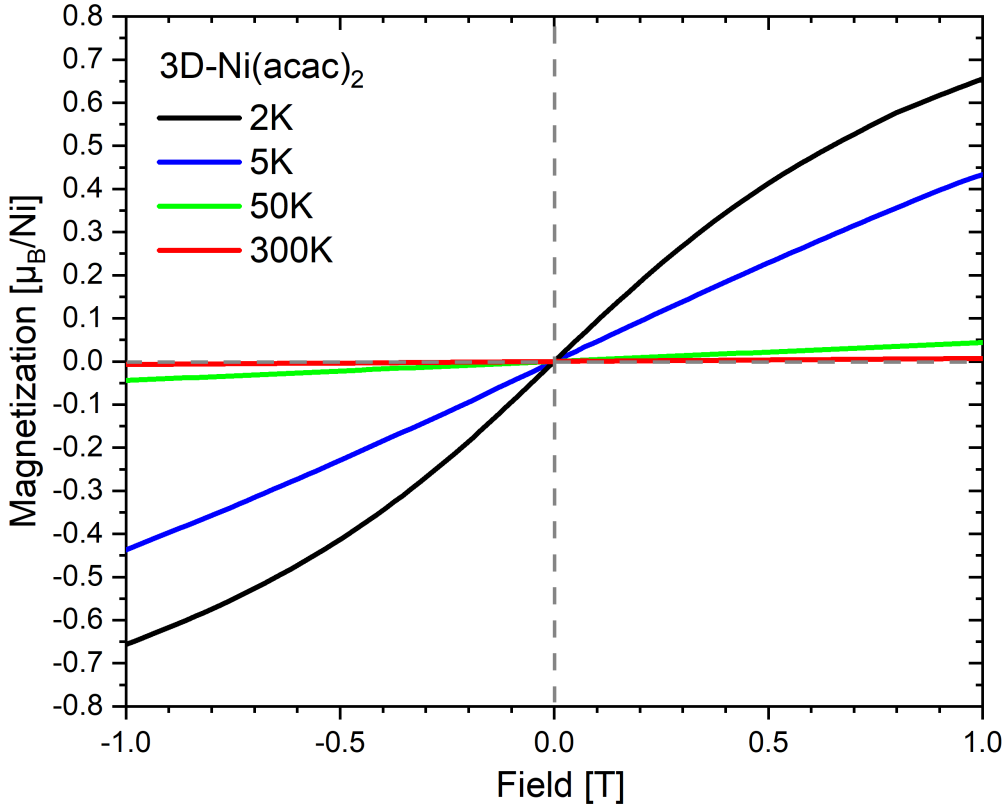

Figure S 6: Field-dependent magnetisation data of the 3D-Ni(acac)$_2$ at 2, 5, 50 and 300K.

4 XPS elemental analysis

Conducting XPS on Ni(acac)$_2$ in ultra-high vacuum conditions is problematic as the molecule sublimes fast in vacuum at room temperature. The encapsulation with SWCNTs allows XPS measurements to be carried out without special cares such as fast sample transferring and cooling.

As shown in Fig. S7, the XPS survey spectra of the Ni(acac)$_2$@NT2.1 and Ni(acac)$_2$@NT1.3 measured with AlK_α radiation exhibit only Ni, C and O peaks (Au peaks are from the substrate used for XPS measurements).

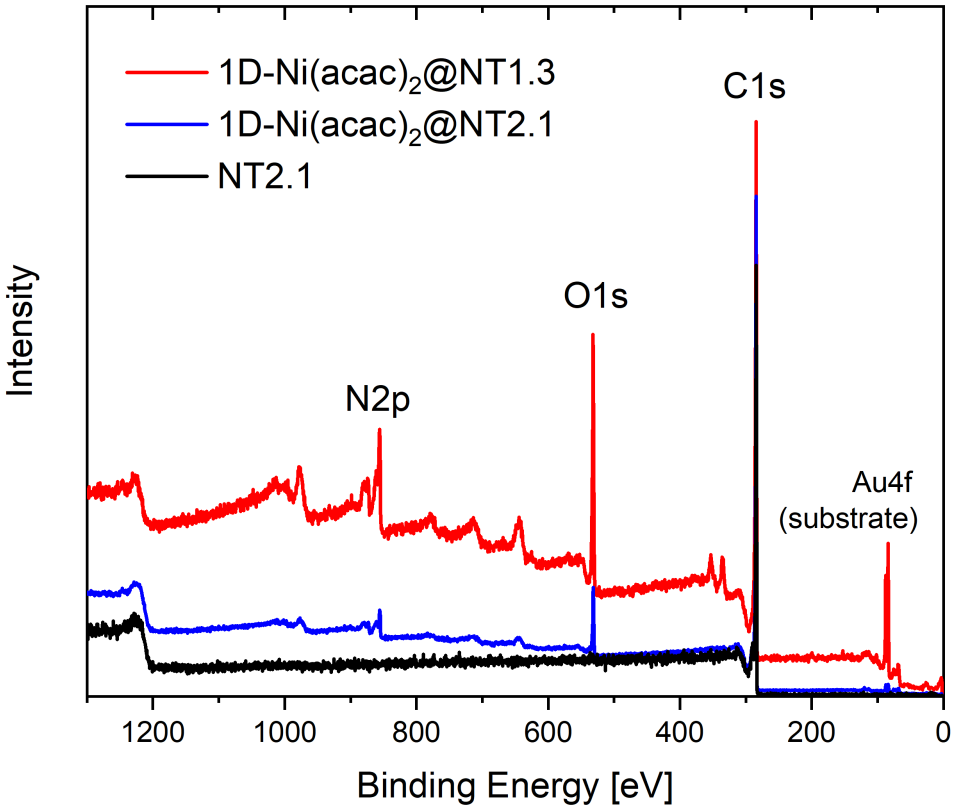

Figure S 7: XPS survey spectra of the NT2.1, Ni(acac)$_2$@NT2.1 and Ni(acac)$_2$@NT1.3.

4.1 Ni2p edge

Figure S8 shows the XPS spectra at the Ni2p and C1s edges recorded for the 1D-Ni(acac)$_2$@NT1.3 and 1D-Ni(acac)$_2$@NT2.1. Both Ni2p spectra in Fig. S8 left exhibit charge transfer satellites[8] typical for Ni(II) in octohedral coordination geometry[9] as observed for the 3D-Ni(acac)$_2$, confirming the sustained molecular structure within the SWCNTs. In the spetrum of 3D-Ni(acac)$_2$ peaks are broader and shifted slightly to a higher binding energy as compared with those of the 1D-Ni(acac)$_2$@NT1.3 and 1D-Ni(acac)$_2$@NT2.1, possibly due to charging during the XPS measurement.

From the area intensity ratio between the Ni2p and C1s edges, the relative atomic concentration can be evaluated by taking the photoionisation cross section into account. We get a Ni/C ratio of 4.3%$_{at}$ for the 1D-Ni(acac)$_2$@NT1.3 and Ni/C=1.5%$_{at}$ for the 1D-

Ni(acac)$_2$@NT2.1. The difference in filling degree can be explained by considering the Van der Waals (VdW) forces acting on the trimers within the nanotube; the most energetically stable and favorable case is when the trimer just fits into the interior of the tube and the separation of the trimer and the tube walls is the VdW distance.

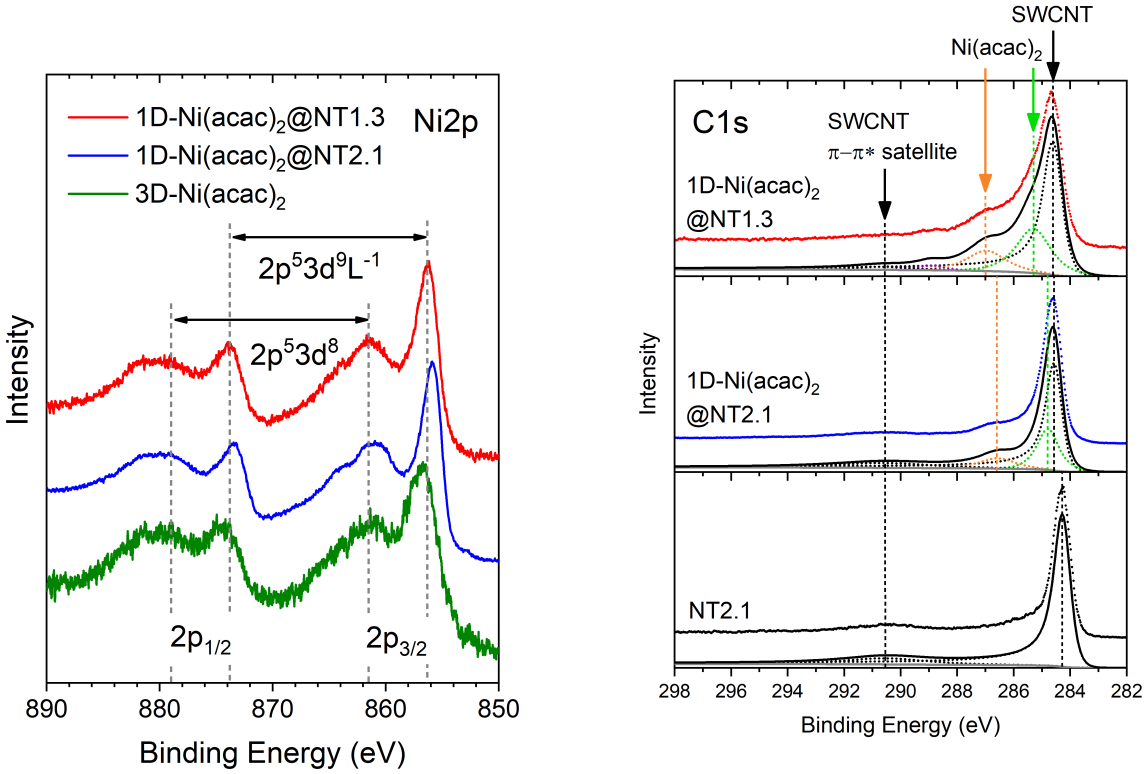

Figure S8: (left) Ni2p XPS data for the 1D-Ni(acac)$_2$@NT1.3, 1D-Ni(acac)$_2$@NT2.1 and 3D-Ni(acac)$_2$ showing a typical spectrum for Ni(II) in octahedral coordination geometry. (right) C1s XPS data for the 1D-Ni(acac)$_2$@NT1.3, 1D-Ni(acac)$_2$@NT2.1 in comparison with unfilled NT2.1. The best-fit curves are plotted below the experimental data together with the peaks of the line shape analysis as the dashed lines.

4.2 C1s edge

In turn, the C1s spectra in Fig. S8 right exhibit broadening and skewing of the main peak and emerging of the high energy components upon filling. The C1s spectrum of the SWCNT reference (NT2.1), representative for both diameters, is fit well by an asymmetric Doniach-

Sunjic function (DS) with an assymetry parameter of $\alpha_{DS} = 0.09$ folded with a Gauss-Laurentian (GL) centered around 284.3eV (FWHM 0.65eV) and a GL function for the $\pi - \pi*$ satellite centered around 290.5eV(FWHM 3.4eV). For the 1D-Ni(acac)$_2$@NT2.1, the main peak is shifted to 284.6eV (FWHM 0.64eV) with no change in asymmetry parameter $\alpha_{DS} = 0.09$. The $\pi - \pi*$ satellite remains at 290.6eV (FWHM 4.1eV). Two additional components centered around 284.8eV (FWHM 0.91eV) and 286.6eV (FWHM 1.5eV) can be attributed to the C1s peaks of the 1D-Ni(acac)$_2$. The Ni(acac)$_2$@NT1.3 has a higher filling degree and thus differs more from the SWCNT reference than the Ni(acac)$_2$NT2.1 does. The main peak's binding energy shifts to 284.6eV (FWHM 0.76eV). The $\pi - \pi*$ satellite at 290.6eV (FWHM 2.4eV) is substantially reduced in intensity. The 1D-Ni(acac)$_2$ carbon peaks are much more pronounced and upshifted to 285.3eV (FWHM 1.4eV) and 287.0eV (FWHM 1.6eV). Table S1 provides an overview of the fitting functions and parameters. The binding energy upshift of the C1s main peak as increasing the filling factor can be attributed to n-type doping of the SWCNTs [3, 10].

Sample	Function and Asymmetry α_{DS}	BE [eV]	FWHM [eV]	Area [%]
NT2.1	(DS*GL) 0.09	284.3	0.65	89.8
	GL	290.5	3.4	10.2
$Ni(acac)_2$@NT2.1	(DS*GL) 0.09	284.6	0.64	63.3
	GL	284.8	0.91	18.8
	GL	286.6	1.5	7.8
	GL	290.6	4.1	10.1
$Ni(acac)_2$@NT1.3	(DS*GL) 0.09	284.6	0.76	63.1
	GL	285.3	1.4	21.5
	GL	287.0	1.6	11.0
	GL	289.0	1.1	1.8
	GL	290.6	2.4	2.6

Table S 1: Fitting parameters for the carbon 1s line of the pristine NT2.1, $Ni(acac)_2$@NT2.1 and $Ni(acac)_2$@NT1.3. DS stands for the Donijac-Sunij function (asymmetry parameter α_{DS}) and GL for a Gauss-Laurentian function. (DS*GL) is the folding of DS with GL.

4.3 Atomic concentration

The chemical formula of dehydrated $Ni(acac)_2$ is $C_{10}H_{16}NiO_4$. Hydrogen atom are invisible due to its small photoionisation cross section and oxygen impurities are known to exist in SWCNTs. Hence, only Ni2p and C1s peaks are used for the following elemental analysis. The area intensities of the Ni2p and C1s peaks, I_{Ni2p} and I_{C1s}, are evaluated after Shirley background subtraction[6]. The number desity of Ni(C) is given as $n_{Ni(C)} = \frac{I_{Ni(C)}}{CS_{Ni(C)}}$, where $CS_{Ni2p(C1s)}$ is the photoionisation cross section of the Ni2p (C1s) state at a photon energy of 1486.6eV [11]. The number ratio of Ni to C is then given as I_x/I_C which is 4.3 at.% for the 1D-$Ni(acac)_2$@NT1.3, 3.3 at.% for the 1D-$Ni(acac)_2$@NT1.7 and 1.5 at.% for the $Ni(acac)_2$@NT2.1.

4.4 Conversion of units for magnetisation

The unit conversion for the magnetisation from emu as measured in SQUID to μ_B/nickel to be compared with XMCD data requires the number of nickel in a Ni(acac)$_2$@NT sample that can be evaluated from XPS data as follows. The mass of a Ni(acac)$_2$@NT sample is given as

$$M^{Ni(acac)_2@NT} = N_{Ni}A^{Ni}+N_CA^C+N_OA^O+N_HA^H = \alpha(n_{Ni}A^{Ni}+n_CA^C+n_OA^O+n_HA^H) \quad (1)$$

where A_X is the atomic mass, N_X the number of element X in the sample, and in the second term n_X is the number density and α is constant. From the chemical formula of dehydrated 1D-Ni(acac)$_2$, $C_{10}H_{14}NiO_4$,

$$n_O = 4n_{Ni}, n_H = 14n_{Ni}. \quad (2)$$

Substituting the above, we get

$$M^{Ni(acac)_2@NT} = \alpha(n_{Ni}A^{Ni}+n_CA^C+4n_{Ni}A^O+14n_{Ni}A^H) = \alpha(n_{Ni}(A^{Ni}+4A^O+14A^H)+n_CA^C). \quad (3)$$

Hence, the number of nickel in the sample is calculated from experimental values n_C, n_{Ni} and $M^{Ni(acac)_2@NT}$ as

$$N_{Ni} = \alpha n_{Ni} = \frac{M^{Ni(acac)_2@NT}}{A^{Ni} + 4A^O + 14A^H + n_C/n_{Ni}A^C}. \quad (4)$$

5 XMCD data analysis

Figure S9 shows the X-ray absorption spectrum (XAS) of the 1D-Ni(acac)$_2$@NT1.7 at the Ni 2p edges, in comparison to the theoretical multiplets (vertical bars) and spectrum (dashed line) of Ni^{2+} in octahedral ligand geometry calculated by using the CTM4XAS program [12].

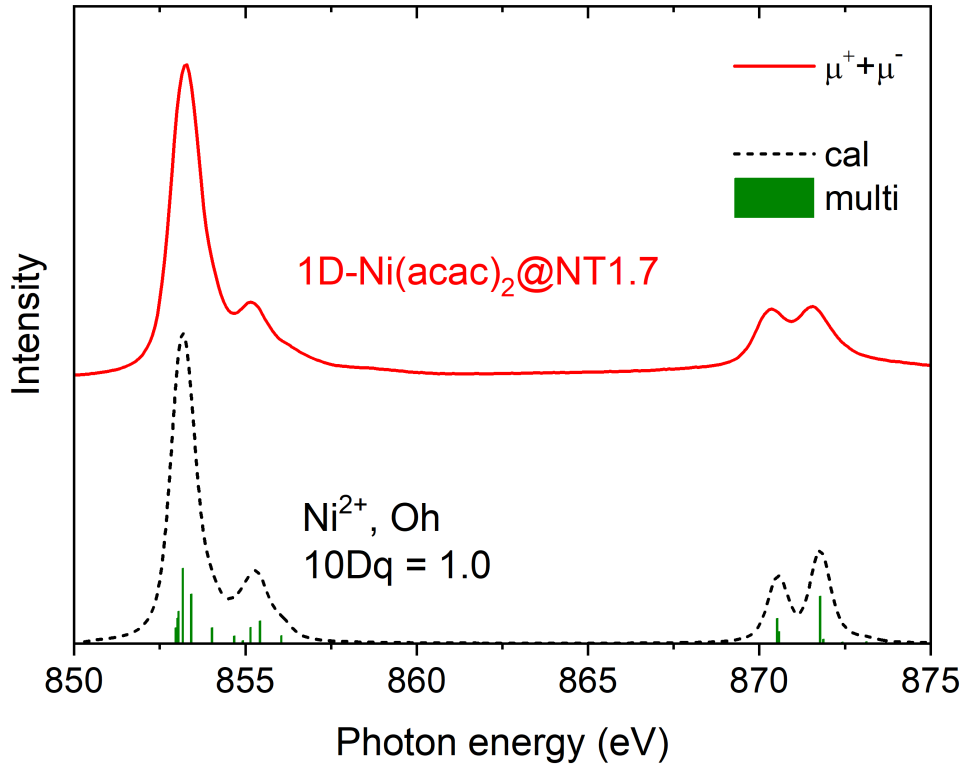

Figure S 9: Experimental XAS (μ^++μ^-) for the 1D-Ni(acac)$_2$@NT1.7 recorded at 4.16K under magnetic fields of ±6T and theoretical XAS (dashed line) simulated for six-coordinated octahedral Ni^{2+} by using the CTM4XAS program [12] with crystal field parameter 10 Dq = 1.0, lorentzian broadening = 0.2 and gaussiuan broadening = 0.2.

Figure S10 shows an example of XMCD data of the 1D-Ni(acac)$_2$@NT1.7 sample. It was recorded at 6T and 4.16K across the nickel L edge. The difference between the two measurements with opposite photon helicitiy μ^+ and μ^- is the XMCD signal. The cumulative intensities of $\mu^+ + \mu^-$ and $\mu^+ - \mu^-$ are evaluated as shown in the inset, giving us the experimental sum rule parameters p, q and r, allowing to determine the orbital and spin magnetic moments m_{orbit} and m_{spin} using the XMCD sum rules[13, 14, 15]:

$$\frac{m_{orbit}}{n_h} = -\frac{4q}{3r} \tag{5}$$

$$\frac{m_{spin} + 7m_T}{n_h} = -\frac{6p - 4q}{r}. \tag{6}$$

The number of 3d holes n_h was set to two. The magnetic dipole term m_T can be omitted [16, 17]. A degree of circular polarization of $90 \pm 2\,\%$ was taken into account.

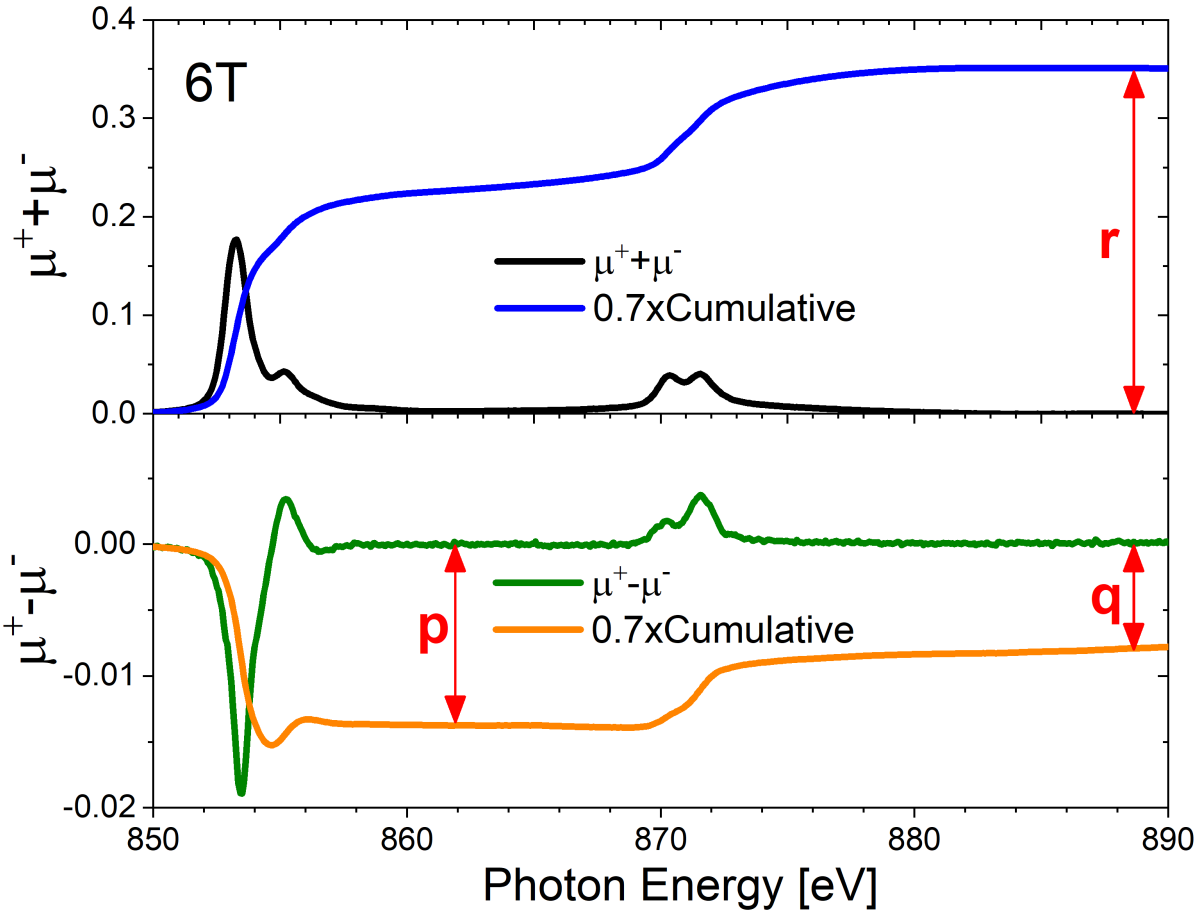

Figure S10: Commutative profiles of XAS (μ^++μ^-) and XMCD (μ^+-μ^-) are plotted in blue. XMCD sum rule parameters p, q and r are indicated. XAS data, μ^+ and μ^-, were recorded at 4.16K under a magnetic field of 6T.

6 Evaluation of exchange parameters

Figure S11a, b and c show the temperature-dependent magnetisation data measured by SQUID at 1T for the 3D-Ni(acac)$_2$, 1D-Ni(acac)$_2$@NT2.1 and 1D-Ni(acac)$_2$@NT1.3, respectively, after subtraction of the SWCNT magnetism. Fitting the data for the 1D-Ni(acac)$_2$@NT2.1 is possible, but with various exchange values. This is due to the negative and positive ex-

change couplings competent with each other, resulting in the low temperature data coinside with the Curie-Weiss line. Hence, the fitting result has not been discussed in the manuscript. It is noticable that both 1D-Ni(acac)$_2$ structures (b and c) exhibit much enhanced Pauli paramagnetism as compared with the 3D-Ni(acac)$_2$ (a).

Fitting the data to Eq. 1 in the manuscript, we get Pauli paramagnetism values of $M_c \sim 0.001$ μ_B/nickel for the 3D-Ni(acac)$_2$, 0.02 μ_B for the 1D-Ni(acac)$_2$@NT2.1 and 0.01 μ_B/nickel for 1D-Ni(acac)$_2$@NT1.3. The data below 5K have been excluded from the fitting as the saturation dominates at 1T, as seen in the field dependent data at 2K (see Fig. S6). Upon fitting we have considered two different cases, case I: $J \geq 0$ and $J_{13} \leq 0$ and case II: $J \leq 0$ and $J_{13} \geq 0$, yielding two different pairs of exchange coupling constants (see Table S2). Then, we have chosen the pair in one of the two cases under the assumption that the nearest-neighbour exchange dominates the other, $|J| > |J_{13}|$. The corresponding fitting curves are inverse-plotted after subtraction of M_c in the inset in Fig. S11a,b and c, alongside with the dashed green curve with zero exchange counplings, $J = 0$ and $J_{13} = 0$, that follows the Curie law.

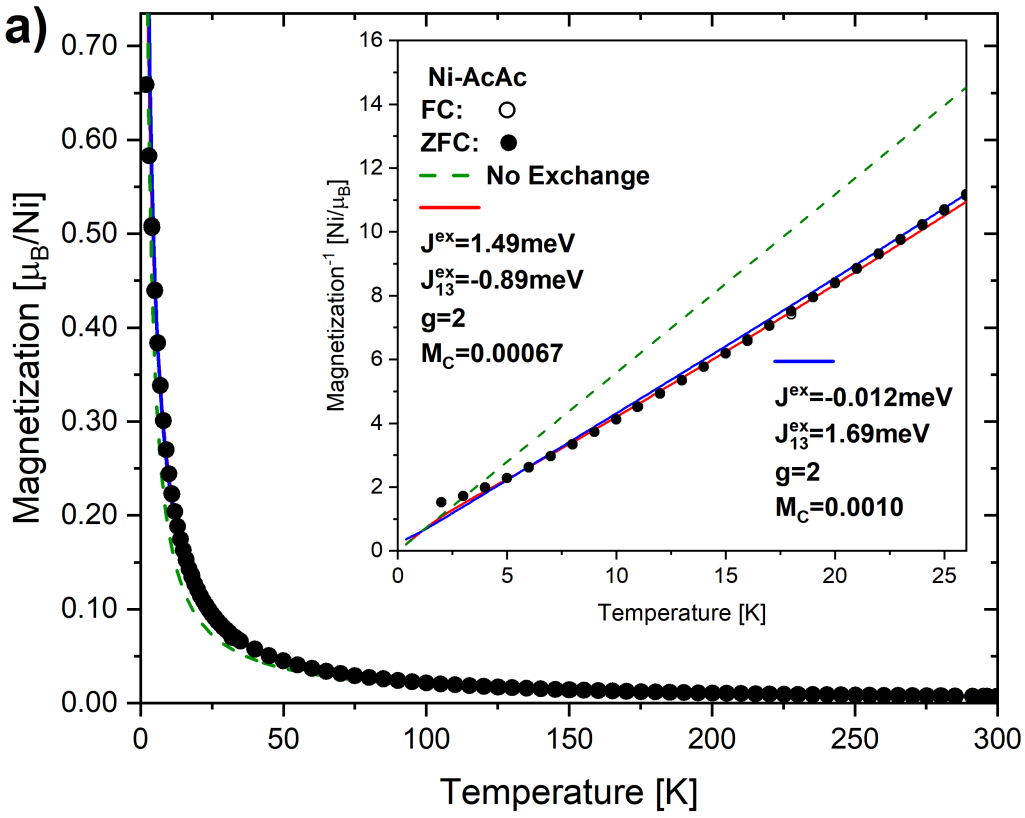
a)
Magnetization [μ_B/Ni]
Temperature [K]
Ni-AcAc
FC:
ZFC:
No Exchange
J^{ex}=1.49meV
J^{ex}_{13}=-0.89meV
g=2
M_C=0.00067
J^{ex}=-0.012meV
J^{ex}_{13}=1.69meV
g=2
M_C=0.0010
Magnetization^{-1} [Ni/μ_B]
Temperature [K]

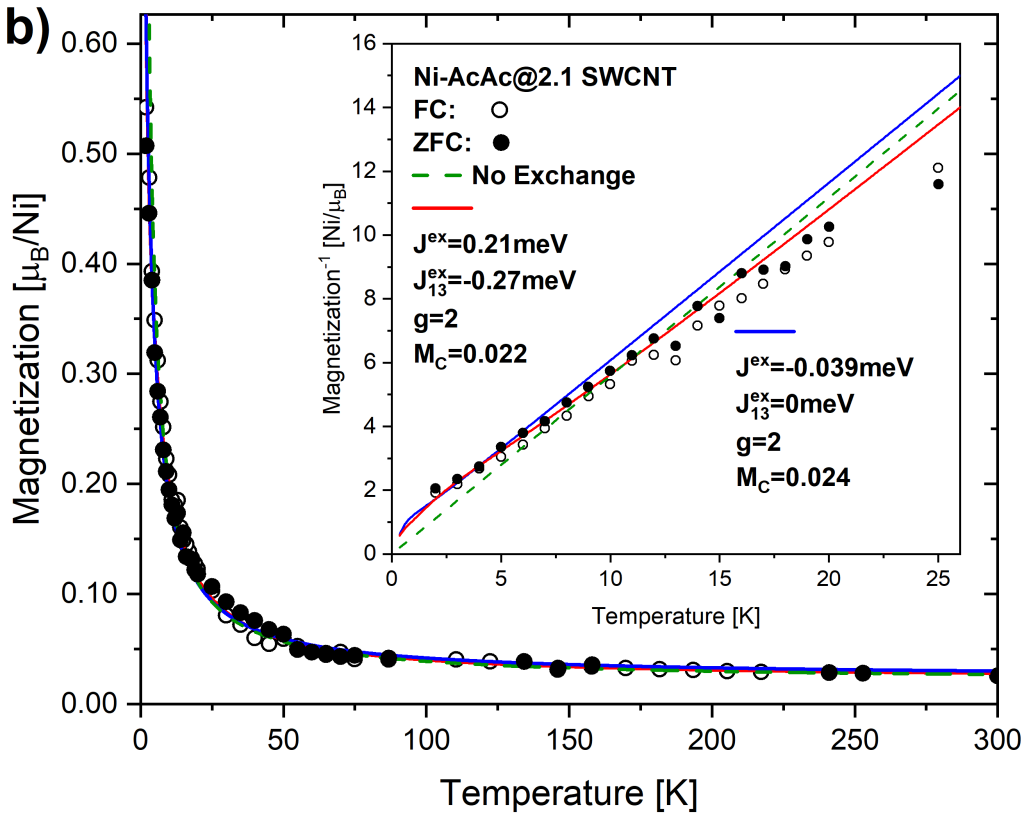
b)
Magnetization [μ_B/Ni]
Temperature [K]
Ni-AcAc@2.1 SWCNT
FC:
ZFC:
No Exchange
J^{ex}=0.21meV
J^{ex}_{13}=-0.27meV
g=2
M_C=0.022
J^{ex}=-0.039meV
J^{ex}_{13}=0meV
g=2
M_C=0.024
Magnetization^{-1} [Ni/μ_B]
Temperature [K]

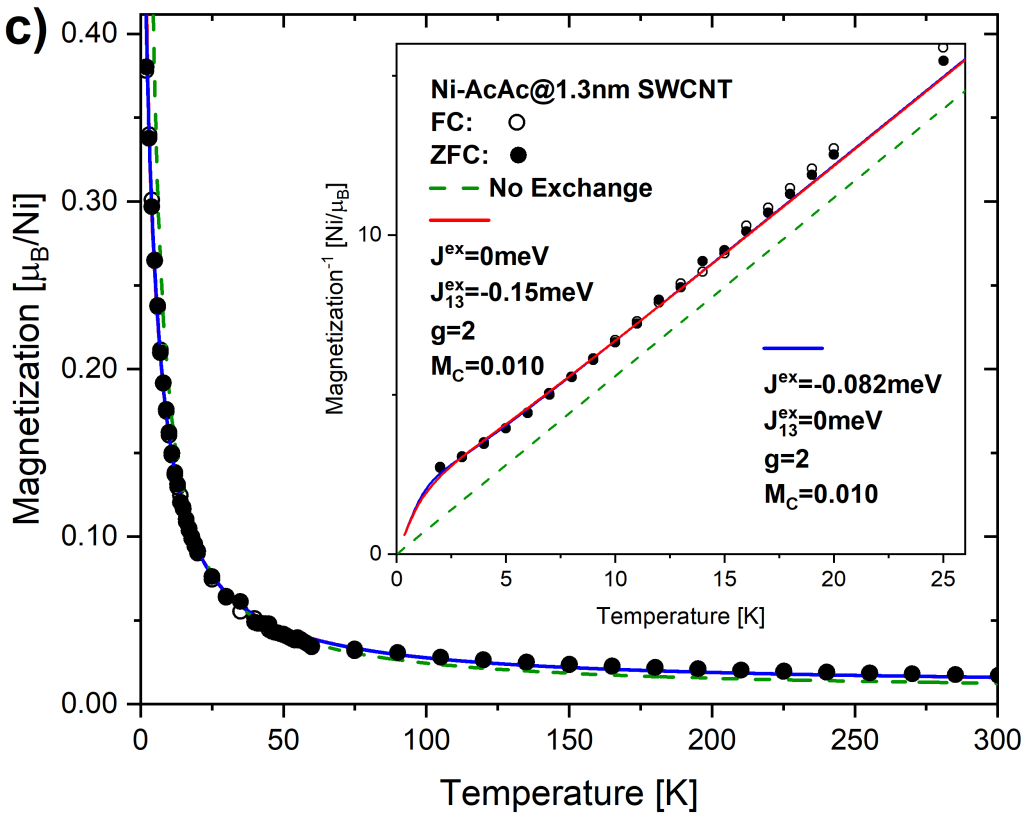

Figure S 11: The magnetisation per nickel atom versus temperature in the range between 2K and 300K measured under a magnetic field of 1T for (a) 3D-Ni(acac)$_2$, (b) 1D-Ni(acac)$_2$@NT2.1 and (c) 1D-Ni(acac)$_2$@NT1.3. The solid and open circles are measured upon zero field (ZFC) and field cooling, respectively. The red and blue curves are the results of fitting the data with Eq. 1 in case I ($J \geq 0$, $J_{13} \leq 0$) and case II ($J \leq 0$, $J_{13} \geq 0$) , respectively. Additionally, the purely paramagnetic curve, Eq. 1 with $J = 0$, $J_{13} = 0$, is plotted. The inset shows the inverse magnetisation data and fitting curves after subtraction of constant magnetisation offset M_c.

Sample & Field	**J [meV]**	**J_{13} [meV]**	**M_c [μ_B/Ni]**
3D-Ni(acac)$_2$ (I)	1.49±3%	-0.89±3%	0.0007±10%
3D-Ni(acac)$_2$ (II)	-0.012±8%	1.69±9%	0.001±13%
1D-Ni(acac)$_2$@NT2.1 (I)	0.21±28%	-0.27±19%	0.022±4%
1D-Ni(acac)$_2$@NT2.1 (II)	-0.039±7%	0	0.022±4%
1D-Ni(acac)$_2$@NT1.3 (I)	0	-0.15±2%	0.010±3%
1D-Ni(acac)$_2$@NT1.3 (II)	-0.082±4%	0	0.010±2%

Table S2: Exchange coupling constant J between the nearest-neighbour spins and J_{13} between the terminal spins evaluated by fitting the temperature-dependent magnetisation data with Eq. 1 with g=2 plus Pauli magnetism M_c.

References

[1] T. Saito, S. Ohshima, T. Okazaki, S. Ohmori, M. Yumura, and S. Iijima. Selective diameter control of single-walled carbon nanotubes in the gas-phase synthesis. *J. Nanosci. Nanotechnol.*, 8(11):6153–6157, 2008.

[2] M. V. Kharlamova, M. Sauer, T. Saito, Y. Sato, K. Suenaga, T. Pichler, and H. Shiozawa. Doping of single-walled carbon nanotubes controlled via chemical transformation of encapsulated nickelocene. *Nanoscale*, 7:1383–1391, 2015.

[3] H. Shiozawa, T. Pichler, A. Gruneis, R. Pfeiffer, H. Kuzmany, Z. Liu, K. Suenaga, and H. Kataura. A catalytic reaction inside a single-walled carbon nanotube. *Adv. Mater.*, 20(8):1443–1449, April 2008.

[4] G. J. Bullen, R. Mason, and Peter Pauling. The crystal and molecular structure of bis(acetylacetonato)nickel (ii). *Inorg. Chem.*, 4(4):456–462, April 1965.

[5] S. Doniach and M. Sunjic. Many-electron singularity in x-ray photoemission and x-ray line spectra from metals. *Journal of Physics C: Solid State Physics*, 3(2):285, 1970.

[6] D. A. Shirley. High-resolution x-ray photoemission spectrum of the valence bands of gold. *Phys. Rev. B*, 5(12):4709–4714, June 1972.

[7] H. Kataura, Y. Kumazawa, Y. Maniwa, I. Umezu, S. Suzuki, Y. Ohtsuka, and Y. Achiba. Optical properties of single-wall carbon nanotubes. *International Conference on Science and Technology of Synthetic Metals*, 103(1):2555–2558, June 1999.

[8] K. Okada, A. Kotani, and B. T. Thole. Charge transfer satellites and multiplet splitting in x-ray photoemission spectra of late transition metal halides. *J Electron Spectros Relat Phenomena*, 58(4):325–343, 1992.

[9] M. A. van Veenendaal and G. A. Sawatzky. Nonlocal screening effects in 2p x-ray photoemission spectroscopy core-level line shapes of transition metal compounds. *Phys. Rev. Lett.*, 70:2459–2462, Apr 1993.

[10] H. Shiozawa, T. Pichler, C. Kramberger, A. Gruneis, M. Knupfer, B. Buchner, V. Zolyomi, J. Koltai, J. Kurti, D. Batchelor, and H. Kataura. Fine tuning the charge transfer in carbon nanotubes via the interconversion of encapsulated molecules. *Phys. Rev. B*, 77(15):153402, April 2008.

[11] J-J Yeh. *Atomic calculation of photoionization cross-sections and asymmetry parameters.* Gordon & Breach Science Publ.; AT&T Bell Laboratories, 1993.

[12] Eli Stavitski and Frank M. F. de Groot. The CTM4XAS program for EELS and XAS spectral shape analysis of transition metal L edges. *MICRON*, 41(7):687–694, OCT 2010.

[13] B. T. Thole, P. Carra, F. Sette, and G. van der Laan. X-ray circular dichroism as a probe of orbital magnetization. *Phys. Rev. Lett.*, 68:1943–1946, Mar 1992.

[14] P. Carra, B. T. Thole, M. Altarelli, and X. Wang. X-ray circular dichroism and local magnetic fields. *Phys. Rev. Lett.*, 70:694–697, Feb 1993.

[15] C. T. Chen, Y. U. Idzerda, H.-J. Lin, N. V. Smith, G. Meigs, E. Chaban, G. H. Ho, E. Pellegrin, and F. Sette. Experimental confirmation of the x-ray magnetic circular dichroism sum rules for iron and cobalt. *Phys. Rev. Lett.*, 75:152–155, Jul 1995.

[16] M. Komelj, C. Ederer, J. W. Davenport, and M. Fahnle. From the bulk to monatomic wires: An ab initio study of magnetism in co systems with various dimensionality. *Phys. Rev. B*, 66(14):140407, October 2002.

[17] S. Peredkov, M. Neeb, W. Eberhardt, J. Meyer, M. Tombers, H. Kampschulte, and G. Niedner-Schatteburg. Spin and orbital magnetic moments of free nanoparticles. *Phys. Rev. Lett.*, 107(23):233401, November 2011.